

# A Reconfigurable On-Board Power Converter for Electric Vehicle With Reduced Switch Count

Soumya Ranjan Meher<sup>ID</sup>, *Student Member, IEEE*, Somenath Banerjee<sup>ID</sup>, *Student Member, IEEE*, Bhanu Teja Vankayalapati, *Student Member, IEEE*, and Rajeev Kumar Singh<sup>DP</sup>, *Senior Member, IEEE*

**Abstract**—This paper proposes a compact reconfigurable on-board power converter for low voltage electric vehicle. The proposed converter serves the purpose of a battery charger as well as a 3-phase voltage source inverter (VSI) to drive the traction motor. The 3-phase VSI is the backbone of this converter that can be either reconfigured to a propulsion unit or to a battery charger by adding few more power electronics components. During charging mode, the topology is reconfigured to form a front-end boost power factor correction rectifier which is cascaded by a DC-DC converter through a DC link. The same power stage is reconfigured to operate as a 3-phase VSI to drive the traction motor during propulsion mode. Thus, it reduces the switch count by eliminating the requirement of a separate inverter stage. Simultaneously the weight, volume, and cost of the overall system are reduced. Unified control technique is implemented which is capable to achieve near-unity power factor operation of front-end boost rectifier as well as optimal battery charging without sensing the DC link voltage. This control scheme implements a single control loop for both stages by eliminating the need of two separate control loop for each stage of the charger. A 470 W scaled-down prototype is developed and its performance is validated with Constant Current-Constant Voltage charging of a 24 V, 30Ah battery pack in charging mode and with a 400W BLDC motor in propulsion mode.

**Index Terms**—Electric vehicles, integrated battery charger, optimal battery charging, PFC, reconfigurable topology.

## I. INTRODUCTION

OPTIMAL design of the power converters plays an important role in the performance of Electric Vehicle (EV). Conventionally, two separate power conversion units are required for the operation of EVs. The charging process of the battery pack is implemented by a battery charger and a propulsion unit drives the traction motor [1], [2]. Based on placement of charger, EV chargers can be categorized into two types viz. on-board and off-board chargers [3]–[6]. Off-board chargers are usually DC chargers capable of handling high-power and are installed at charging stations for fast charging. Relatively lower powered on-board chargers are installed within the vehicle. On-board

Manuscript received July 16, 2019; revised November 19, 2019; accepted January 11, 2020. Date of publication February 11, 2020; date of current version April 16, 2020. This work was supported by the Department of Science and Technology, Government of India, IIT(BHU), under Grant DST/CERI/MI/SG/2017/086. The review of this article was coordinated by Dr. A. Khaligh. (*Corresponding author: Soumya Ranjan Meher*)

The authors are with the Department of Electrical Engineering, Indian Institute of Technology (BHU), Varanasi, U.P., India (e-mail: soumyaramehers.eee17@iitbhu.ac.in; somenathbanerjee.eee17@iitbhu.ac.in; bvx180006@utdallas.edu; rksingh.eee@iitbhu.ac.in).

Digital Object Identifier 10.1109/TVT.2020.2973316

chargers are preferred because the EV can be charged from a standard AC outlet [7]. However, as an on-board charger is integrated into the vehicle itself, its power density must be maximized. Also, as the cost of the on-board charger adds to the vehicle's overall cost, its reduction is important from an economic standpoint [8].

In conventional EVs, there is an inverter to drive the traction motor from battery and a separate on-board charger to charge from the grid supply. But as charging and driving are mutually exclusive operations, the same power electronics hardware can be utilized for both the operations thus reducing the switch count. This approach saves costs and improves the power density of the on-board system. The idea of integrating the traction inverter with battery charger for EVs has been studied widely in recent publications [9]–[11].

In [12] an integrated charger topology is presented which uses the drive system of an EV to charge the battery from a single phase or a 3-phase AC source. This topology is suitable only for high voltage battery packs since the battery is directly connected to the output of the rectifier in charging mode. [13] presents an integrated battery charger using an Interior Permanent Magnet motor with access to the neutral connection of the star connected winding. An E-Scooter using an onboard bidirectional DC-DC converter and a high voltage battery pack (260 V) is used for validation. In [14], the charger is integrated with the propulsion system. The motor windings act as boost inductor as well as the power semiconductor switches are reutilized during charging mode. However, it requires three phase power supply and it is meant for high power applications. Paper [15] discusses about a two-stage on-board battery charger. The first stage is an interleaved boost topology used for power factor correction and the second stage is a full bridge LLC topology used as DC-DC converter. This work is also aimed at high voltage battery packs. Multiphase machine based on-board battery chargers are also discussed [16]–[21]. Such machines are not generally used in applications like e-scooters, electric motorcycles, etc., due to the machine size and large switch count necessary in the inverters. Literature [22] presents an onboard DC-DC converter targeted at plug-in hybrid electric vehicles. The battery charging feature is integrated with the converter. The application of the topology with respect to pure electric vehicles is limited to the context of vehicles with powertrain consisting of a DC-DC stage.

The topologies reported so far are effective for high voltage battery packs (300 V–400 V). But EVs such as electric scooters, motorcycles, e-rickshaws, and golf carts have power trains

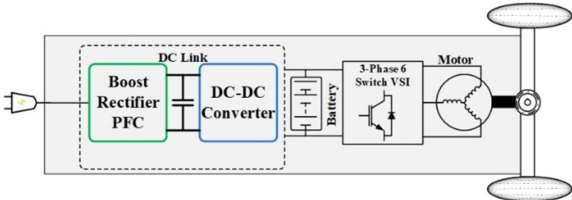


Fig. 1. Conventional charger topology for charging low voltage battery packs.

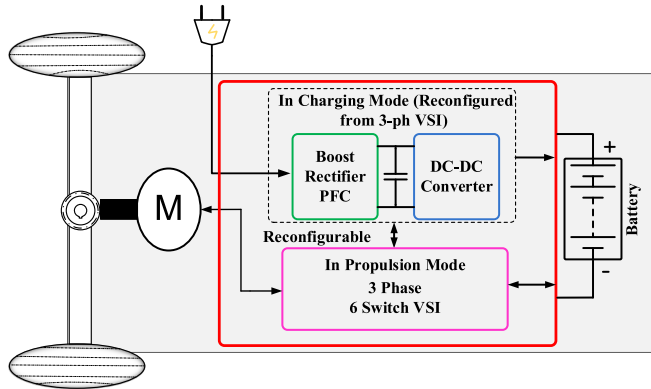


Fig. 2. Proposed reconfigurable integrated battery charger.

that work on lower voltage battery packs (24 V–110 V). The conventional powertrain architecture of the low voltage EVs is shown in Fig. 1.

It may be observed from Fig. 1 that for battery charging, typically two power stages are used, namely: 1) boost rectifier power factor correction (PFC) stage for near-unity power factor operation on input side and 2) step down DC-DC conversion stage to step down the front-end converter output voltage to a level suitable for charging the battery. Further, it is also clear from Fig. 1 that a voltage source inverter (VSI) is needed to drive the motor of EVs.

This paper proposes a single converter topology, which can be reconfigured into a 3-phase VSI during propulsion mode and an EV battery charger during charging mode. In propulsion mode, the converter transfers power from the battery to the traction motor. During charging mode, the same converter is reconfigured to obtain a two-stage battery charger consisting of a boost rectifier power factor correction (PFC) stage and a DC-DC converter stage sharing a common DC link. Thus, in the proposed topology, the 6 switch-VSI is reconfigured as a charger for optimal charging of a low voltage battery pack during charging mode and as an inverter to drive the electric traction motor during propulsion mode. This enables the integration of the charger with the drive unit of a low battery voltage EV, which leads to reduction in weight, volume, and cost of the overall system for such vehicles. The schematic of the proposed topology is shown in Fig. 2. The two boxes indicating the modes of operation of the converter represents the reconfigurable nature of the topology. Hence the two boxes indicating two different converters are effectively amalgamated into one reconfigurable converter represented by the red box. The battery and the motor along with the axle as present in a traditional electric vehicle are illustrated in Fig. 2.

Further, a unified control scheme is implemented for the control of the front-end PFC stage and the DC-DC converter in charging mode using a single control loop. Hence the need for separate control loops for each of the power stages is eliminated. This eases the design process and also saves computational resource.

Overall contribution of the paper is summarized as follows:

- 1) This paper proposes a reconfigurable on-board power converter (R-OPC) for low voltage EVs. The proposed R-OPC uses a 3-phase, 6 switch VSI in the powertrain that can be reconfigured as boost rectifier front-end PFC converter cascaded with DC-DC converter to give optimal constant current-constant voltage (CC-CV) charging of the battery during charging mode. During propulsion mode, the same R-OPC is reconfigured to drive the electric motor of low voltage Electric Vehicles. Thus, it reduces the switch count by eliminating the requirement of an additional inverter unit.
- 2) The proposed topology enables integration of battery charging functionality into the drive unit of low battery voltage EVs hence reducing the weight, volume and cost of the powertrain.
- 3) A unified control scheme is implemented for the proposed topology. The control scheme is capable of controlling the PFC stage as well as performing optimal CC-CV charging of the battery through the DC-DC converter with a single control loop. Thus, it eliminates the need of separate control loops for the PFC and the DC-DC converter stages thereby simplifying the design of the system.

The paper is organised as follows. Section II discusses the systematic derivation of the proposed topology. Operating principle in every modes of operation is elaborated in Section III. Section IV discusses overall control strategy and the design criteria. The proposed concept is verified through experimental results in Section V. The paper is concluded in Section VI.

## II. DERIVATION OF THE TOPOLOGY

The motivation for the reconfiguration is to integrate a battery charger into the drive unit of an EV such that the charger obtained is a two-stage converter with a boost rectifier input PFC stage followed by a DC-DC converter with the two sharing a common DC link. Since a 3-phase, 6-switch VSI is widely used for driving the traction motor, it could be considered as the starting point in deriving the EV charger. A 3-phase VSI has 3 half bridge switch legs; hence in the charging mode these legs have to be reassigned for AC-DC boost rectifier and DC-DC conversion operations. Fig. 3 shows the derivation of the integrated battery charger from a 3-ph VSI fed traction motor. The 3-phase VSI legs  $L_1$  and  $L_2$  are operated as asymmetrical two-device unidirectional boost converter. The remaining leg  $L_3$  is used to construct a half-bridge LLC converter for the DC-DC stage.

Two of the motor phase windings connected in series as shown in Fig. 3 and act as the boost inductor at the input side of the AC-DC rectifier stage. Only PH<sub>1</sub> and PH<sub>2</sub> windings of the motor are used during charging mode, while phase c winding remains idle. The charging time period is significantly less as compared to its corresponding motoring duration, and hence its effect in

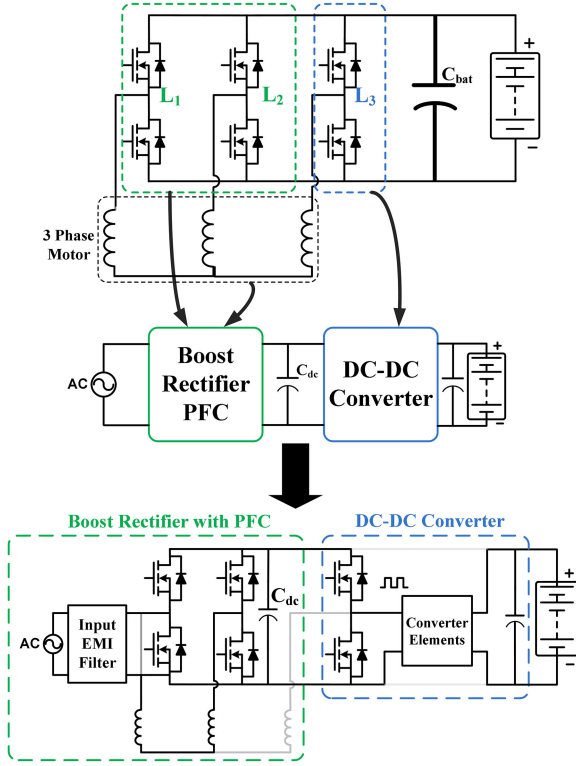


Fig. 3. Derivation of the integrated battery charger from a 3-ph VSI fed traction motor.

the life time of the motor for the above stated reason is very less. However, litz wire can be used for designing windings to further increase the life time of the motor.

The DC-DC converter includes a centre-tapped transformer with leakage inductance  $L_t$  and magnetizing inductance  $L_m$ , a resonant capacitor  $C_r$  and diodes  $D_1$  &  $D_2$ .  $L_t$  and  $L_m$  can be utilized as the resonant components of the LLC resonant network [23]. A DC link capacitor is used between the two converter stages to maintain the DC link voltage constant.

The motor windings are re-utilized as the boost inductance in the charging mode. The voltage rating of the motor is proportional to the back emf generated which is generally proportional to the number of stator winding turns of a motor. The number of winding turns determines the winding inductance. This implies that the winding inductance of low voltage motors can be low. Low input inductance can result in considerable input current ripple. Addition of external inductance on the input side in series with the motor phase windings might be necessary to mitigate the high ripple.

The R-OPC topology must be reconfigured into a two-stage single-phase battery charger from a 3-phase VSI and vice-versa. Thus, a switching mechanism is needed for mode transition. Five electromechanical contactors (Form-1C) are used for this purpose while deriving the topology as shown in Fig. 4. Form 1-C contactors have 3 contacts; 1. CM (Common contact), 2. NC (Normally closed contact) 3. NO (Normally open contact) as shown in Fig. 4. When the electromagnetic coil is unenergized, the CM contact is connected to the NC while the NO is kept opened. Energizing the coil toggles the connection of CM from NC to NO.

The reconfiguration topology effectively reduces the number of switches as the need of a separate VSI for propulsion unit is eliminated. Table I. compares the switch count of various EV battery charger topologies presented in literature with the proposed topology.

### III. MODES OF OPERATION

#### A. Propulsion Mode

The circuit configuration in propulsion mode is shown in Fig. 5. In this mode, the fixed contacts of all the contactors are connected to their respective NC positions. Contactors  $C_1$  and  $C_2$  isolate the system from the grid and also connect the motor phase  $PH_1$  winding to leg  $L_1$ . Similarly, contactors  $C_3$  and  $C_4$  isolate the DC link capacitor and connect the 3-phase inverter bridge to the battery pack. The contactor  $C_5$  isolates the LLC resonant network and closes the motor phase 3 winding with leg  $L_3$  to complete the 3 phase VSI. The diodes  $D_1$  and  $D_2$  are reverse biased and thus prevents current flow through the secondary of the transformer and hence eliminating the requirement of additional contactors.

#### B. Charging Mode

In the charging mode, all the contactors are energised to connect their common contacts with corresponding normally open (NO) positions as shown in Fig. 6. Contactor  $C_1$  connects one lead from the grid supply to leg  $L_1$  of the topology. Contactor  $C_2$  connects the other lead from grid to the leg  $L_2$  of the 3-phase inverter bridge through  $PH_1$  and  $PH_2$  motor windings. Contactor  $C_3$  and  $C_4$  isolate the battery pack and connect the DC link capacitor to the 3-phase inverter bridge. Contactor  $C_5$  isolates the motor winding  $PH_3$  of the motor and connects to the LLC resonant circuit as shown in Fig. 6.

Motor phase windings  $PH_1$  and  $PH_2$  are in series and function as the boost inductors on the input side. The switches  $S_5$  and  $S_6$  are used to construct the half bridge LLC resonant stage. Diodes  $D_1$  and  $D_2$  rectify the secondary side. The battery is charged optimally using the CC-CV charging method.

Switches  $S_2$  and  $S_4$  are switched during the positive and negative half-cycles of the supply voltage respectively. Among the four switches,  $S_2$  and  $S_4$  are switched since low side switching is more convenient. In positive half cycle of supply voltage, body diodes of switches  $S_1$  and  $S_4$  are forward biased and switch  $S_2$  is switched according to the PWM control scheme. Similarly, during negative half cycle, body diodes of switches  $S_2$  and  $S_3$  are forward biased and the switch  $S_4$  is switched according to the PWM control scheme.

The operation of AC-DC rectifier as a boost PFC converter during charging mode is explained by four sub modes. During submode-1, current flows through switch  $S_2$  and the body diode of switch  $S_4$  to charge the boost inductor in positive half cycle of supply voltage as shown in Fig. 7(a). In submode-2, the inductor energy is supplied to the DC link through the body diodes of switches  $S_1$  and  $S_4$  to complete the boost operation as shown in Fig. 7(b). Similarly, submode-3 and submode-4 are shown in Fig. 7(c) and Fig. 7(d) respectively for negative half cycle of the supply voltage.

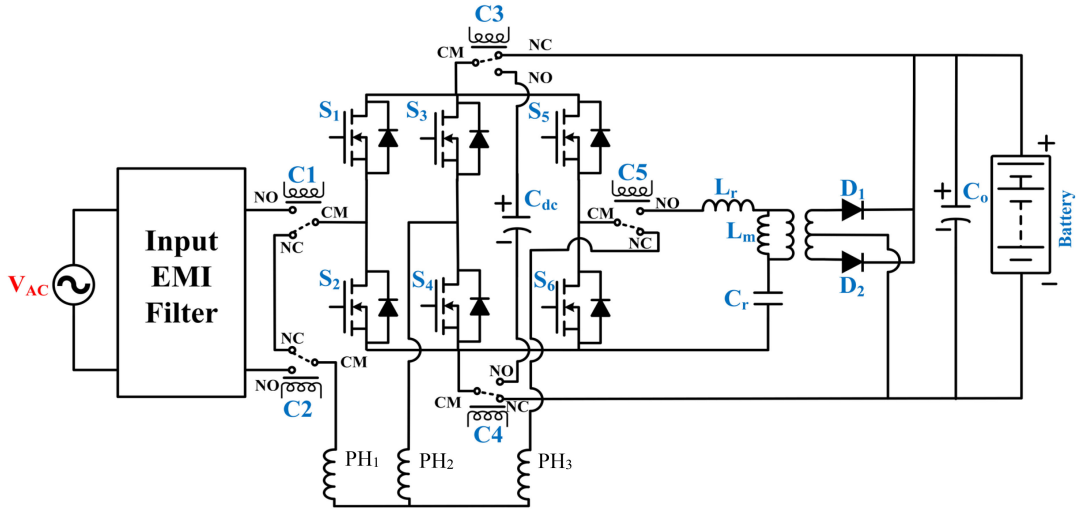


Fig. 4. Final reconfigurable on-board power converter (R-OPC) topology.

TABLE I  
COMPARISON OF SWITCH COUNT OF AVAILABLE LITERATURES WITH THE PROPOSED CONVERTER

Literature	Nature of Supply	No. of stages for battery charging	Galvanic isolation	No. of MOSFETs / IGBTs	No. of Diodes	Requirement of separate 3-phase VSI unit for propulsion (6 additional switches)	Total no. of switches
[13]	1-Phase AC	2	NO	6	4	NO	10
[14]	3-Phase AC	1	NO	12	6	NO	18
[15]	1-Phase AC	2	YES	6	10	YES	22
[24]	1-Phase AC	1	NO	6	4	NO	10
[25]	3-Phase AC	2	NO	9	12	NO	21
Proposed	1-Phase AC	2	YES	6	2	NO	8

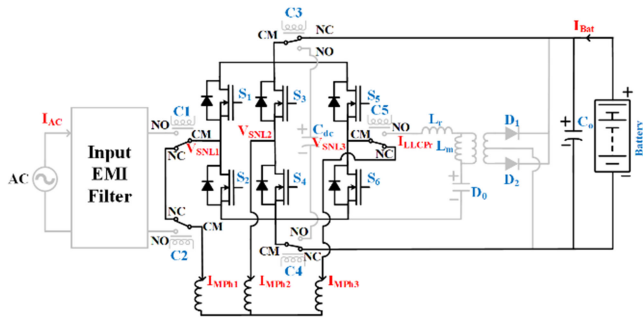


Fig. 5. Circuit configuration in propulsion mode.

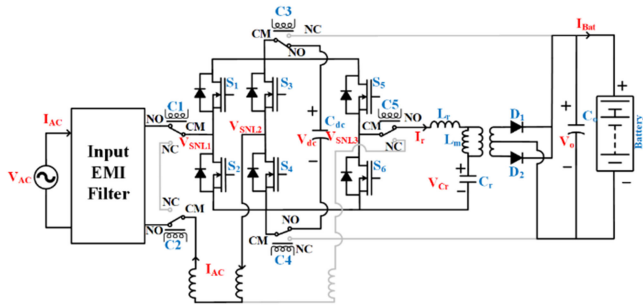


Fig. 6. Circuit configuration in charging mode.

The DC-DC converter stage uses a half bridge LLC resonant converter cascaded with a centre-tapped full-wave rectifier. This stage serves the purpose of galvanic isolation as well as stepping down the DC link voltage.

### C. Mode Switching

The proposed R-OPC must reconfigure from a 3-phase VSI to a two-stage battery charger and vice-versa during mode transitions. Ideally the process of reconfiguration should be executed instantaneously. However, the energy storing elements in the power stage are responsible for continuation of current conduction through contactors. An attempt to switch the contactors may lead to formation of arc between the contacts. To avoid this situation, the current must be allowed to decay. However, a finite time interval is required for the current to decay. The switching instants of the contactors are accordingly sequenced to ensure zero current operation.

During charging to propulsion (C-P) transition, the gate signals of the switches  $S_1 - S_6$  are terminated initially. The AC source current  $I_{ac}$  requires a finite time interval to cease flowing due to the inductance  $L_{in}$  as illustrated in Fig. 8.

The instant of termination of charging mode is denoted by  $t_x$  and the corresponding source current is denoted by  $i_x$ . The time

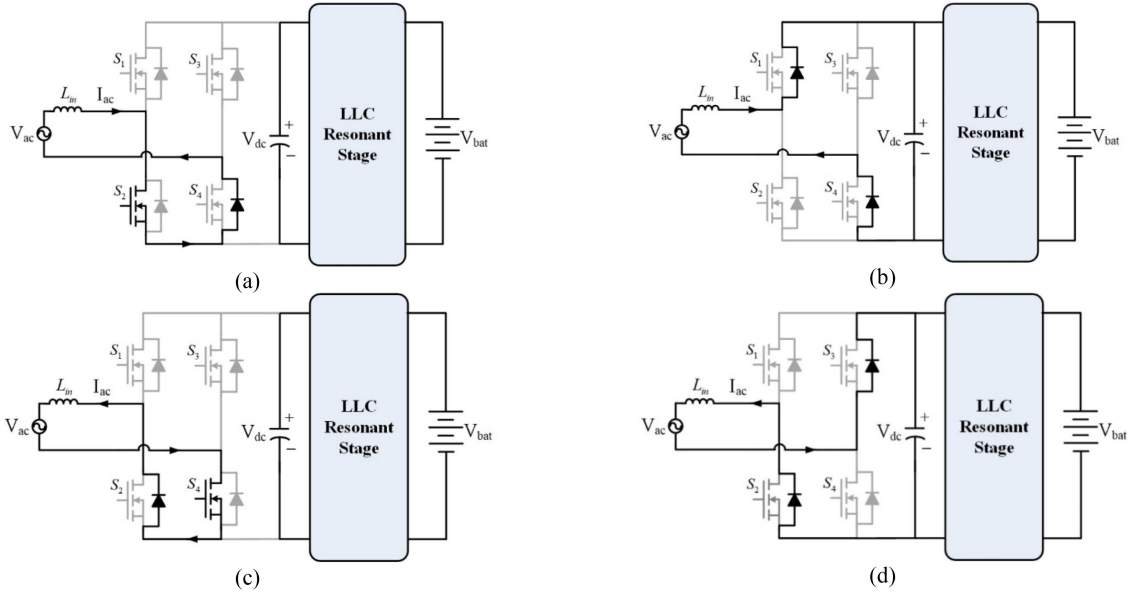


Fig. 7. Modes of operation of boost PFC stage: during positive half-cycle: (a)  $S_2$  is ON (submode-1); (b)  $S_2$  is OFF (submode-2); and during negative half-cycle: (c)  $S_4$  is ON (submode-3); (d)  $S_4$  is OFF (submode-4).

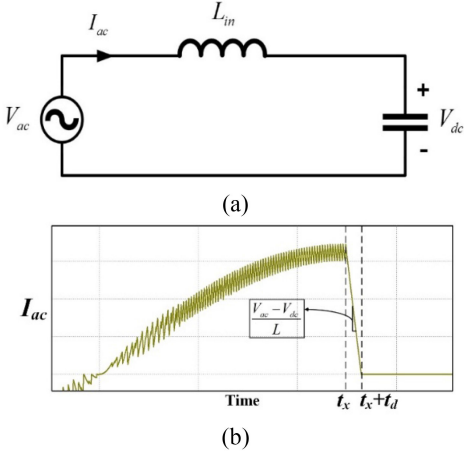


Fig. 8. (a) Equivalent circuit of input stage with switches  $S_1$ - $S_4$  turned off and anti-parallel body diodes of  $S_1$  and  $S_4$  forward biased. (b) Source current waveform during C-P transition.

required for the source current to decay completely is denoted by  $t_d$ . The dynamics of the source current  $I_{ac}$  during this period can be expressed as,

$$L \frac{di_{ac}}{dt_d} = V_{ac} - V_{dc} \quad (1)$$

where,

$$V_{ac} = V_m \sin(\omega t) \quad (2)$$

It is observed from (1) that the slope of decay of the source current is not constant over time due to the sinusoidal nature of grid voltage. Integrating (1), we can derive an expression of time  $t_d$ . For the sake of simplicity, one positive half cycle is considered for analysis which is generalized later. Since the charger operates at near-unity power factor, the source current  $I_{ac} = I_m \sin(\omega t)$ .

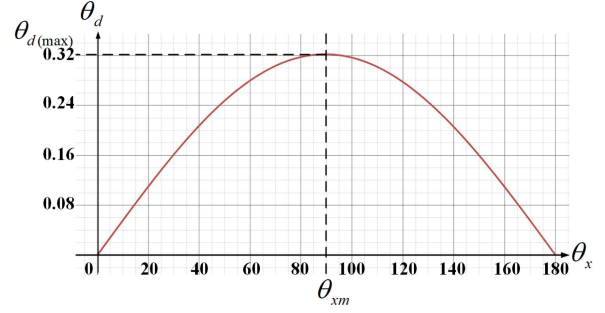


Fig. 9. Graphical representation of the relation between turn-off angle and delay angle.

Representing the phase angle in terms of degrees, we may express (1) as,

$$\omega L \frac{di_{ac}}{d\theta_x} = V_m \sin \theta - V_{dc} \quad (3)$$

Integrating (3) and simplifying,

$$\begin{aligned} \int_{i_x}^0 \omega L di_L &= \int_{\theta_x}^{\theta_x + \theta_d} (V_m \sin \theta - V_{dc}) d\theta - \omega L I_m \sin \theta_x \\ &= [-V_m \cos \theta - V_{dc} \theta]_{\theta_x}^{\theta_x + \theta_d} V_m \cos(\theta_x + \theta_d) \\ &\quad - V_m \cos \theta_x - \omega L I_m \sin \theta_x + V_{dc} \theta_d = 0 \end{aligned} \quad (4)$$

The implicit relation of  $\theta_x$  and  $\theta_d$  is plotted graphically for the range 0 to 180 degrees in Fig. 9.

It is evident from the Fig. 9 that the maximum delay angle occurs when the phase angle of the source current is at 90 degrees. Equation (1) holds true for both positive and negative half cycles of the source current. Thus, the analysis performed for the positive half cycle is valid over the period of the source current. Generalizing the inference, it can be stated that the

TABLE II  
SWITCHING STATES OF VSI BASED ON HALL EFFECT SENSORS OUTPUT

Sectors	Position of PM magnetic axis	Outputs of Hall effect Sensors			Switching States					
		H <sub>1</sub>	H <sub>2</sub>	H <sub>3</sub>	S <sub>1</sub>	S <sub>2</sub>	S <sub>3</sub>	S <sub>4</sub>	S <sub>5</sub>	S <sub>6</sub>
I	330° < θ ≤ 30°	1	0	0	OFF	OFF	ON	OFF	OFF	ON
II	30° < θ ≤ 90°	1	1	0	OFF	ON	ON	OFF	OFF	OFF
III	90° < θ ≤ 150°	0	1	0	OFF	ON	OFF	OFF	ON	OFF
IV	150° < θ ≤ 210°	0	1	1	OFF	OFF	OFF	ON	ON	OFF
V	210° < θ ≤ 270°	0	0	1	ON	OFF	OFF	ON	OFF	OFF
VI	270° < θ ≤ 330°	1	0	1	ON	OFF	OFF	OFF	OFF	ON

time interval  $t_d$  is maximum when  $|\sin(\omega t_x)| = 1$ . Hence, the resulting equation involving the maximum decay time  $t_{d(\max)}$  can be derived as,

$$\begin{aligned} \int_{I_m}^0 L di_{ac} &= \int_{t_x}^{t_x + t_{d(\max)}} (V_{ac} - V_{dc}) dt \\ \frac{V_m}{\omega} \cos \omega(t_{d(\max)} + t_x) + V_{dc} t_{d(\max)} \\ - \frac{V_m}{\omega} \cos \omega t_x - LI_m \sin \omega t_x &= 0 \end{aligned} \quad (5)$$

Considering the condition  $|\sin(\omega t_x)| = 1$  and with relevant information of source voltage, current and frequency, (5) can be solved for  $t_{d(\max)}$ .

The contactors C<sub>1</sub>, C<sub>2</sub>, C<sub>3</sub> and C<sub>4</sub> are accordingly switched after time  $t_{d(\max)}$  from the instant of termination of charging mode. The current in LLC resonant network is terminated immediately since the switches S<sub>5</sub> and S<sub>6</sub> are turned off and the corresponding anti-parallel body diodes gets reverse biased. Hence, contactor C<sub>5</sub> can be switched without any time delay.

During propulsion to charging (P-C) transition, as soon as the vehicle reaches standstill condition, the motor phase currents cease to flow. Hence all of the contactors can be switched instantaneously.

Zero current switching of the contactors are ensured by following the switching sequence derived from the above analysis. Hence, no switching loss occurs during the switching operation of the contactors. However, the contactors must be rated to conduct the respective branch currents and should be capable of blocking the voltage difference between respective nodes during both modes of operation. Considering these factors, contactors of form 1-C controlled by an electrically energized coil are used for this purpose. The electromechanical contactors are given preference over solid state devices since this application does not need high frequency switching for mode transition operation. Moreover, the contactors are also cheaper than the similarly rated solid-state devices.

#### IV. CONTROL AND DESIGN ANALYSIS

##### A. Control Scheme for Propulsion Model

A conventional propulsion model was used to drive the BLDC motor during propulsion mode. The BLDC motor used in this prototype comes with three inbuild binary hall effect sensors

which are positioned symmetrically at a distance of 120° among them. Such an arrangement results in a 60° resolution measurement. Thus, the entire cycle of 360° is divided into six equal sectors, each of 60°. The sensor outputs are used to sense the position of the permanent magnet (PM) flux density wave. Consequently, the switching states are determined according to Table II.

##### B. Control Scheme for Charging Model

The topology is reconfigured as per Fig. 6 during charging. The first stage serves the purpose of an AC/DC boost rectifier, which additionally takes care of the input power factor correction. The objectives of the second stage are to provide galvanic isolation during charging from the grid, ensure soft switching to minimize switching losses and step down the DC link voltage for low voltage battery pack. Considering these factors, the LLC resonant converter is chosen as the second stage DC-DC converter.

The half-bridge converter topology is shown in Fig. 10. In order to ensure ZVS at the switches, the switch current must lag the voltage across the switches. Hence, the input impedance of the LLC network ( $Z_i$ ) as seen from the terminals AA' must be inductive in nature [26]. The input impedance ( $Z_i$ ) as seen from the terminals AA' with resistance R connected across BB' can be expressed as,

$$Z_i = \frac{s^3 L_m L_r C_r + s^2 (L_m + L_r) C_r R + s L_m + R}{s^2 L_m C_r + s C_r R} \quad (6)$$

where,

$L_r$  is the series inductance

$L_m$  is the parallel inductance

$C_r$  is the resonant capacitance

$R$  is the resistance across terminals BB'.

The bode diagrams of  $Z_i$  for varying load conditions are shown in Fig. 11. It is observed from Fig. 11 that  $f_{sc}$  is the resonant frequency when BB' is short circuited and  $f_{oc}$  is the resonant frequency when BB' are open circuited. The poles are dominant on frequencies lower than  $f_{oc}$  and zeroes are dominant on the frequencies higher than  $f_{sc}$ . Hence, it can be implied that the input impedance is inductive in nature at frequencies higher than  $f_{sc}$  for all load conditions. Therefore, to ensure ZVS, the switching frequency ( $f_s$ ) of the half-bridge LLC converter must be greater than or equal to  $f_{sc}$ .

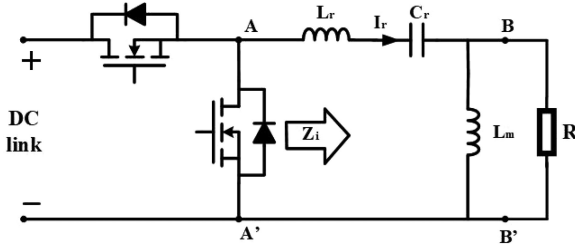
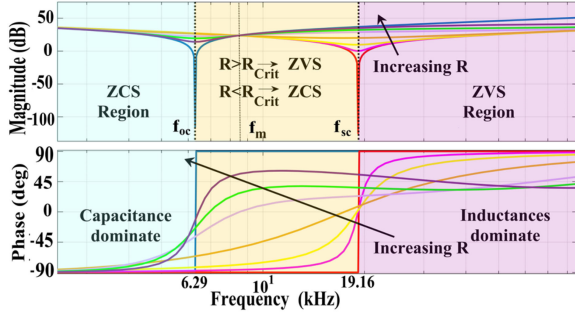


Fig. 10. Half-bridge LLC resonant converter.

Fig. 11. Bode diagrams of  $Z_i$  for varying load condition.

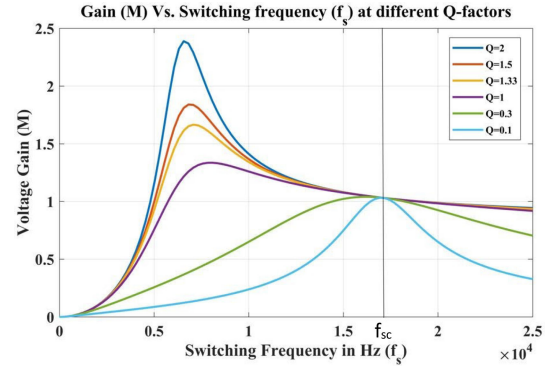
The resonant converter also achieves soft switching which increases the efficiency of the converter. However, the soft switching is ensured through proper designing of the resonant tank elements. Traditional design process of the LLC converter presents several challenges due to the fact that LLC converters perform power conversion by frequency modulation instead of pulse width modulation, hence requiring a different design approach. Conventional methods such as steady state averaging method works satisfactorily with pulse width modulation but have proven unsuccessful with resonant converters. Different methods have been reported to mathematically model the LLC resonant converter [27], [28]. They either do not capture the dynamics over the full range of operation or are mathematically complex. Another frequently used method is to obtain an experimental frequency response plot of the converter to design the controller [29]. This approach requires a test prototype to be built before the controller can be designed. Hence, the First Harmonic Approximation (FHA) method is widely used for resonant converter design. The approximation remains valid in the vicinity of the short circuit resonant frequency ( $f_{sc}$ ). Through this approximation, the non-linear non-sinusoidal circuit is converted to a linear sinusoidal circuit. The voltage gain of the converter can therefore be expressed as follows.

$$g_{LLC} = \frac{jX_{lm}\|R}{(jX_{lm}\|R) + J(X_{lr} - X_{cr})} = \left| \frac{j\omega L_m\|R}{j\omega L_m\|R + j\omega L_r + \frac{1}{j\omega C_r}} \right| \quad (7)$$

Further the output terminal voltage can be expressed as follows.

$$V_o = g_{LLC} * \frac{1}{n} * \frac{V_{in}}{2} \quad (8)$$

where  $n$  is the transformer turns ratio.

Fig. 12. Gain vs frequency curve of half-bridge LLC resonant converter at different  $Q$ -factors.

Normalizing the frequency with  $f_{sc}$  as base, we can write  $f_n = \frac{f_{sw}}{f_{sc}}$ . The ratio of the magnetizing inductance to the leakage inductance is expressed as  $L_n = \frac{L_m}{L_r}$ . The quality factor of the circuit is defined as follows.

$$Q = \frac{1}{R} \sqrt{\frac{L_r}{C_r}} \quad (9)$$

Thus, (7) can be rewritten as follows.

$$g_{LLC} = \left| \frac{L_n f_n^2}{[(L_n + 1)f_n^2 + 1] + j[(f_n^2 - 1)]f_n Q_c L_n} \right| \quad (10)$$

In order to achieve line regulation and load regulation, the converter must be designed for a range of  $g_{LLC}$  which contains the maximum and minimum required gain, defined as  $g_{LLCmax}$  and  $g_{LLCmin}$ .

As observed from Fig. 12, the  $Q$  factor decides the peak gain of the converter. Higher the  $Q$  factor, lower the peak gain that can be attained. Hence, to achieve peak gain  $g_{LLCmax} > 1$ , there must a maximum  $Q$  factor ( $Q_{max}$ ). If  $Q > Q_{max}$ , the maximum gain of the converter is less than  $g_{LLCmax}$ , which results in unfulfillment of design requirements. Generally, at high power ratings, the load is high which implies that  $R$  is very low. From (9), it can be inferred that at high load conditions, the  $Q$  factor tends to be high. This imposes limitations on the gain of the converter. Hence, as a counter measure,  $L_r$  must be reduced. It is thus evident that resonant converters demand low leakage inductance at higher power ratings. However, this observation is valid for converters operating under frequency modulation to achieve the required load regulation. In the proposed work, the converter is designed to operate at only  $f_{sc}$  where it provides unity gain for all  $Q$  factors as observed from Fig. 12. The DC link voltage is regulated to achieve the required load regulation. Consequently, the design of the resonant components is free from  $Q$  factor and magnetizing to leakage inductance ratio which are generally the constraints in the design process. The switching frequency selected initially to be 20 kHz in this case, where the derating of the ceramic capacitor is negligible. Subsequently, the transformer is designed for a magnetizing to leakage inductance ratio of around 8. The measured magnetizing and leakage inductances are found to be 571  $\mu$ H and 69  $\mu$ H respectively. The switching frequency of the converter must be equal to  $f_{sc}$  which

is expressed as follows.

$$f_{sc} = \frac{1}{2\pi\sqrt{L_r C_r}} \quad (11)$$

The resonant capacitor is thus selected according to the following expression such that  $f_{sc}$  is around 20 kHz.

$$C_r = \frac{1}{(2\pi f_{sc})^2 L_r} \quad (12)$$

The capacitor is selected from standard values to be 1  $\mu$ F and the corresponding resonant frequency is calculated to be 19.16 kHz.

It is observed that the gain of the converter at the short circuit resonant frequency remains constant for different  $Q$ -factors. Hence, if the resonant network is switched at the short circuit resonant frequency, it behaves as a proportional block. ZVS for all load conditions is also ensured at  $f_{sc}$  as discussed above. It is observed from Fig. 4 that galvanic isolation and rectification of the output of LLC network is provided by a full wave rectifier with centre-tapped transformer. This configuration inherently provides a gain of 0.5. Furthermore, the half-bridge configuration of the LLC converter also provides a gain of 0.5. Therefore, the effective gain of the second stage is given by,

$$g_s = \frac{1}{4} n g_{LLC} \quad (13)$$

where,

$n$  is the turns ratio of transformer.

$g_{LLC}$  is the gain of LLC resonant network.

The gain of the LLC network ( $g_{LLC}$ ) at the short circuit resonant frequency is unity as observed in Fig. 12. Therefore, the gain of the second stage (DC-DC stage) is given by,

$$g_s = \frac{1}{4} n \quad (14)$$

It can be implied from (14) that the gain of the second stage can be designed by selecting suitable transformer turns ratio. Thereafter, the battery terminal voltage is controlled by varying the DC link voltage [30].

The voltage error to the PFC voltage loop is obtained by comparing the output of the LLC resonant stage with the output reference instead of sensing the DC link voltage. A gain term  $1/g_{LLC}$  is introduced to compensate the proportional gain term of LLC resonant converter ( $g_{LLC}$ ).

The output capacitor is selected based on its usage during charging mode. The value of the capacitor is calculated to minimize the ripple content of the output voltage. The output voltage ripple of a full-wave diode rectifier is given as,  $V_{\text{ripple}} = \frac{I_{\text{ripple}}}{2*f*C}$ . The C value is found to be 1.739 mF considering an output voltage ripple of 0.3% at a switching frequency of 19.16 kHz. As per best available choice in the laboratory, a 2 mF electrolytic capacitor is chosen for the purpose.

It is worth observing that since the second stage acts as a proportional block, it does not require a separate control loop. Hence, the two-stage battery charger can be controlled by a unified control loop as shown in Fig. 13. The control loop implements two PI controllers and ensures near-unity power

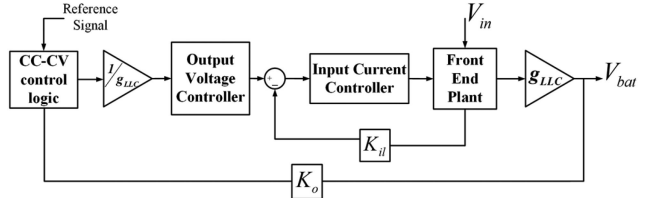


Fig. 13. Implementation of Unified control scheme for the proposed topology.

factor operation as well as optimal battery charging. Charging current and battery terminal voltage are also regulated during constant current and constant voltage modes of battery charging, respectively. Three standard optimal battery charging techniques are reported in the literature [31]–[33]. They are 1) CC-CV charging, 2) pulse charging, and 3) reflex charging. Among these three, CC-CV charging technique is the most popular one and also widely used in the industry. Therefore, in this paper, the CC-CV charging method is adopted to implement the optimal battery charging of EV for the developed prototype.

## V. EXPERIMENTAL VALIDATION

The proposed R-OPC is validated with a 24 V, 400 W BLDC motor and  $2 \times 12$  V, 30 Ah lead acid batteries. Fig. 14 shows the overall implementation of the proposed R-OPC. Considering the size and weight, E-core EE6527 with manganese-zinc ferrite material CF139 is used as the transformer core. The minimum number of primary turns is taken to be 10 for maximum battery terminal voltage of 48 V and unity turns ratio. The primary winding leakage inductance ( $L_r$ ) and the magnetizing inductance ( $L_m$ ) are measured to be 69  $\mu$ H and 571  $\mu$ H, respectively.

The datasheet for the selected core material shows the core loss is minimal for switching frequencies less than 20 kHz.

Using (12), the resonant capacitance is calculated to be 1  $\mu$ F for switching frequency of 19.16 kHz. A TI TMS320F28335 digital signal processor is used to implement the digital controller. Table III lists the components used in the prototype and Fig. 15 shows the photograph of the developed prototype of the proposed R-OPC. The performance of R-OPC is validated in both charging and propulsion mode.

The prototype is tested at its rated power on a 470 W resistive load and also optimally (CC-CV) charging the 24 V, 30 Ah lead acid battery.

### A. Experimental Validation

1) *R-OPC During Propulsion Mode of Operation:* The operation of R-OPC in propulsion mode is validated with a 400 W, 24 V BLDC motor driven by a 24 V battery pack. Fig. 16 shows the motor phase voltages during propulsion mode where battery voltage  $V_{\text{bat}} = 24$  V. It may be observed from Fig. 16 that the BLDC motor phase voltages are phase displaced by  $120^\circ$ . Fig. 17 depicts the motor phase currents  $I_{\text{MPH1}}$ ,  $I_{\text{MPH2}}$  and  $I_{\text{MPH3}}$ . The phase currents are also displaced by  $120^\circ$ . Experimental results shown in Fig. 16 and Fig. 17 validate the performance of the R-OPC in propulsion mode with 400 W, 24 V BLDC motor.

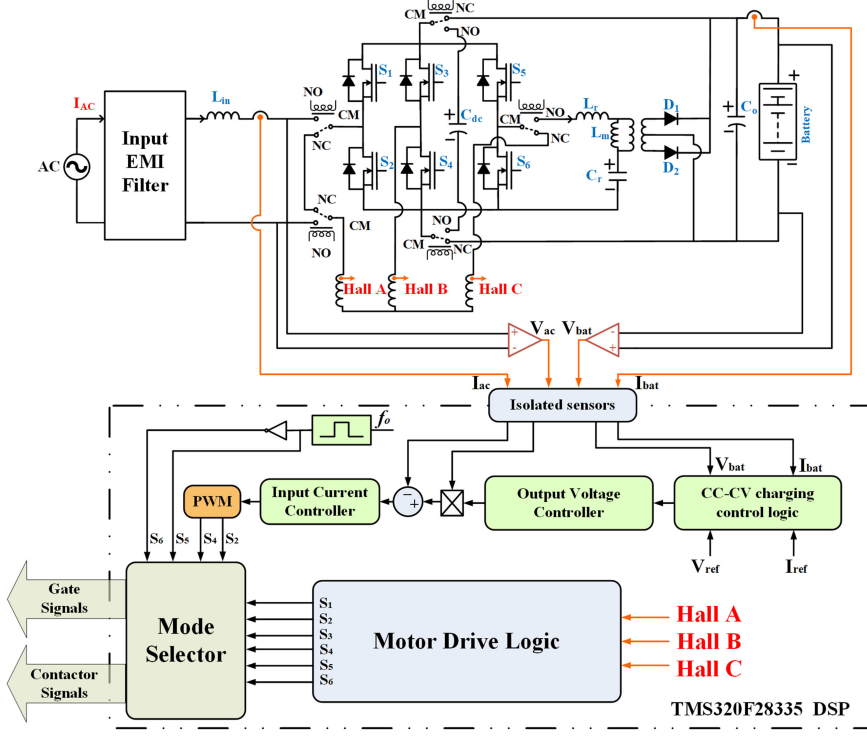


Fig. 14. Complete proposed topology with control scheme.

TABLE III  
COMPONENTS USED WITH RATING

Component	Rating
DC Link Capacitor	1500 $\mu$ F
Output Capacitor	2000 $\mu$ F
MOSFET	500 V/20 A
Diode	200 V/20 A
Transformer	$L_m = 571 \mu H$ , $L_r = 69 \mu H$ , $n = 1$
Motor	400 W, 3-Phase BLDC
Contactor	400 V, 15 A
Resonant Capacitor	1 $\mu$ F, 250 V
Batteries	2x12 V, 30 Ah
Voltage Sensor	320 mV
Current Sensor	20 A

2) *R-OPC During Charging Mode of Operation:* The proposed R-OPC is reconfigured as a two-stage battery charger. It is experimentally tested at its rated power of 470 W for source voltage of 124 V (rms), source current of 5.9 A (rms), battery terminal voltage of 48 V (DC), charging current of 9.71 A. Fig. 18 verifies the PFC operation of R-OPC acting as a boost

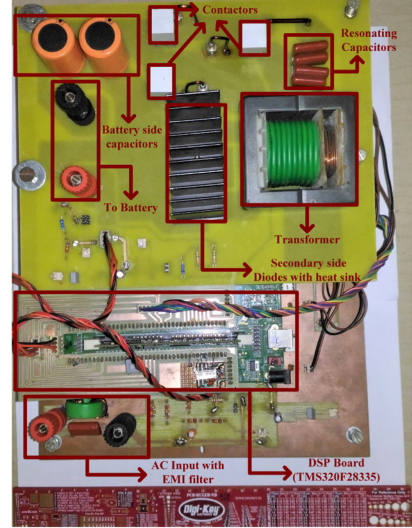


Fig. 15. Photograph of the experimental prototype.

rectifier. It may be observed from Fig. 18 that for AC source voltage  $V_{ac} = 352$  V (peak to peak), a dc link voltage  $V_{dc}$  of 209 V is obtained. The output voltage  $V_0$  is 48 V and the output current is 9.71 A.

Fig. 19 shows that for  $V_{DC} = 104$  V,  $I_{LLC} = 1.64$  A (rms),  $V_{L3}$  varies between 0 V to 104 V, and the voltage across the resonant capacitor  $V_{cr} = 14.85$  V (rms). The figure verifies ZVS turn on of the switches in leg  $L_3$ .

Fig. 20 shows a load transition from 4.855 A to 9.71 A when the input AC voltage and current are 123 V (rms) and 3.54 A (rms), respectively. The result exhibits satisfactory

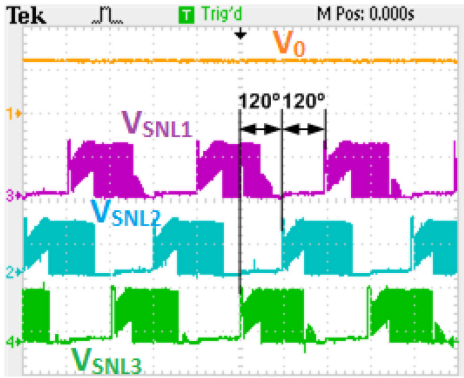


Fig. 16. Three phase BLDC motor operation verified by switch node voltages  $V_{SNL1}$ (CH3),  $V_{SNL2}$ (CH2),  $V_{SNL3}$ (CH4) and battery voltage  $V_{bat}$  (CH1) of the R-OPC (at 120° phase difference) in propulsion mode. (CH1 20 V/div, CH2 20 V/div, Ch3 20 V/div, CH4 20 V/div).

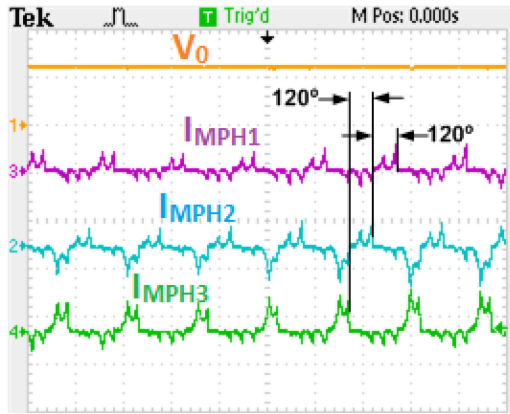


Fig. 17. 3-phase operation of BLDC motor verified by motor phase currents  $I_{MPH1}$ (CH3),  $I_{MPH2}$ (CH2),  $I_{MPH3}$ (CH4) and battery terminal voltage  $V_{bat}$  (CH1) of the R-OPC (at 120-degree phase difference) in propulsion mode. (CH1 20 V/ div, CH2 20 A/div, CH3 20 A/div, CH4 20 A/div).

performance in terms of near-unity power factor operation and smooth transition during sudden change in load. Fig. 21 depicts the motor winding currents along with the supply voltage during the charging mode. In charging mode, motor windings  $PH_1$  and  $PH_2$  are series connected along with an external inductor to increase the boost inductance to a significant value. The currents  $I_{MPH1}$  and  $I_{MPH2}$  are in phase opposition while current  $I_{MPH3}$  during charging mode is zero. Fig. 22 shows the switch node voltage  $V_{L1}$  along with the dc link voltage and output voltage  $V_0$ . It is clear from Fig. 22 that  $V_{L1}$  is switching between the common terminal and DC link voltage where  $V_{DC} = 209$  V and  $V_0 = 50$  V. The voltage stresses across the switches  $S_2$  and  $S_4$  are shown in Fig. 23 for 209 V DC link voltage. The experimental results shown in Fig. 16 to Fig. 23 confirm the operation of the R-OPC in charging mode for a 470 W prototype.

3) *Optimal Charging of 24 V-30 Ah Lead Acid Battery With R-OPC:* CC-CV charging of a 24 V-30 Ah lead acid battery is performed by the R-OPC. It is evident from Fig. 24 that the source voltage  $V_{ac}$  and current  $I_{ac}$  are in phase resulting in unity power factor operation during battery charging. Further, it

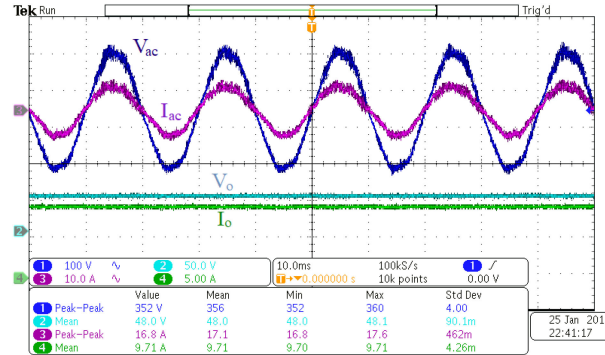


Fig. 18. Steady-state waveforms of 470 W prototype: input voltage ( $V_{ac}$ ) = 352 V (peak-peak), output voltage ( $V_o$ ) = 48 V, input current ( $I_{ac}$ ) = 16.8 A (peak-peak), output current ( $I_o$ ) = 9.71 A.

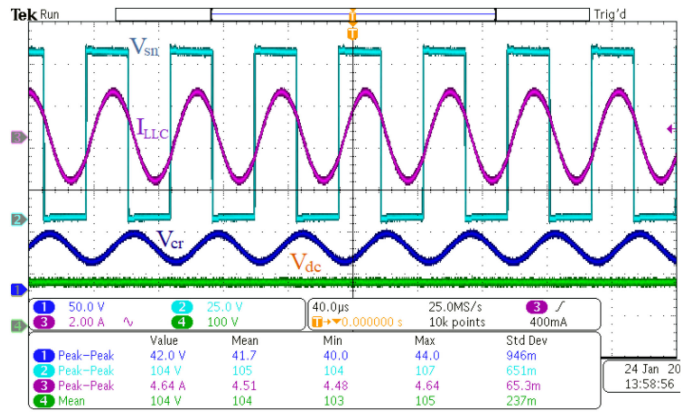


Fig. 19. Steady state waveforms of LLC converter: resonant capacitor voltage ( $V_{cr}$ ) = 42 V (peak-peak), Switch node voltage across  $S_6$  ( $V_{sn}$ ) = 104 V(peak-peak), Current through LLC network ( $I_{LLC}$ ) = 4.64 A(peak-peak), DC link voltage ( $V_{dc}$ ) = 104 V.

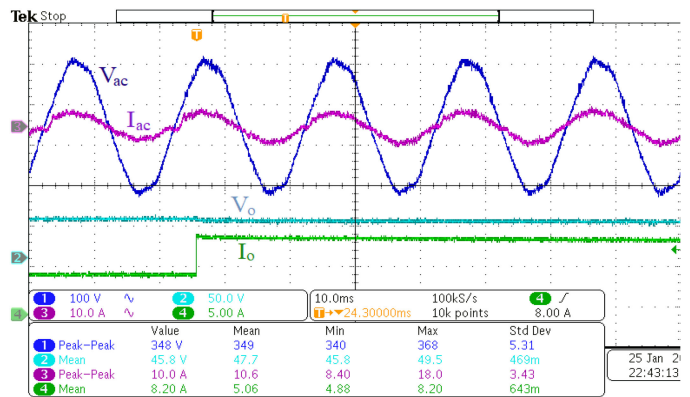


Fig. 20. Dynamic response during charging for 50% increase in load current.

may also be noticed from Fig. 24 that the output current  $I_o$  is regulated at 5.52 A. Fig. 25 shows the experimentally obtained charging profile of 24 V-30 Ah lead acid battery. The battery is charged with constant current (CC) for low battery state of charge (SOC) and as soon as battery voltage reaches 28.7 V, it is charged with constant voltage (CV). The proposed R-OPC

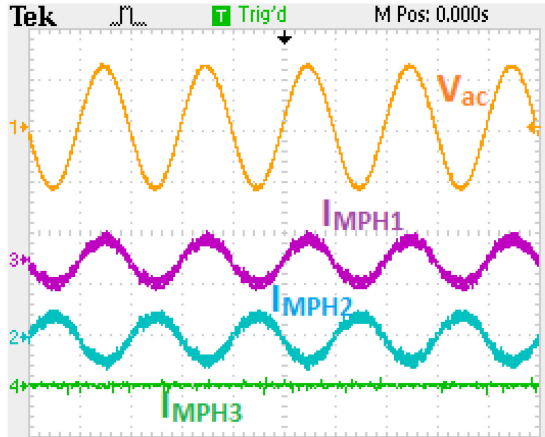


Fig. 21. Motor phase 1(CH3), phase 2(CH2) and phase 3(CH4) currents along with input voltage in charging mode. (CH1 50 V/div, CH2 20 A/div, CH3 20 A/div CH4 20 A/div).

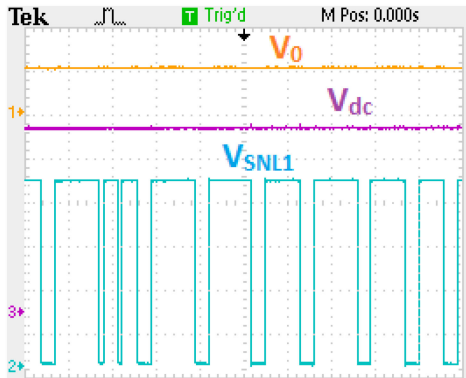


Fig. 22. Voltage stress across switch  $S_2$  in charging mode at 470 W resistive load. (CH1 50 V/div, CH2 50 V/div, CH3 50 V/div).

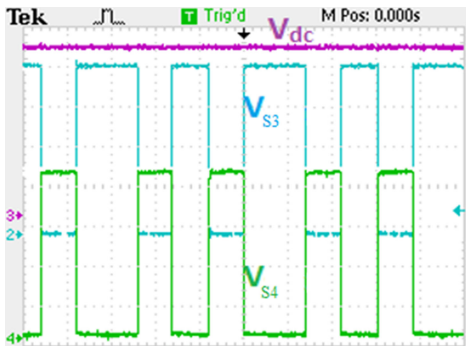


Fig. 23. Switch node voltages  $V_{SNL1}$ (CH2) and  $V_{SNL2}$ (CH4) at 470 W resistive load. (CH2 50 V/div, CH3 50 V/div, CH4 50V/div).

also facilitates smooth transition from CC to CV. The results in Fig. 24 and Fig. 25, confirm the performance of the R-OPC for optimal (CC-CV) charging of a battery. During battery charging, the load at the output terminal varies gradually according to the state of charge (SOC) of the battery. Accordingly, the input power factor of the converter and the Total Harmonic Distortion (THD) of current drawn from the supply changes gradually.

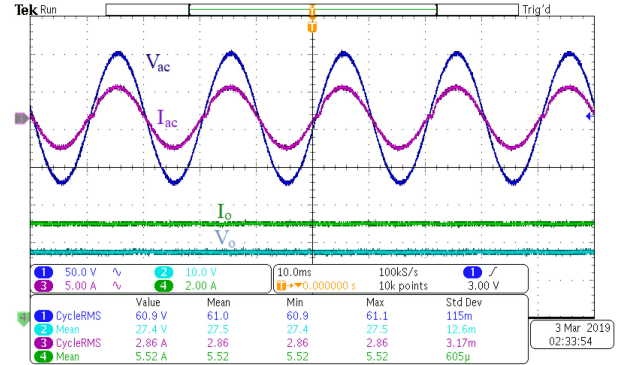


Fig. 24. R-OPC operation during charging of 24 V, 30 Ah lead acid battery. Depicted waveforms of source voltage (CH1), battery terminal voltage (CH2), source current (CH3) and charging current (CH4).

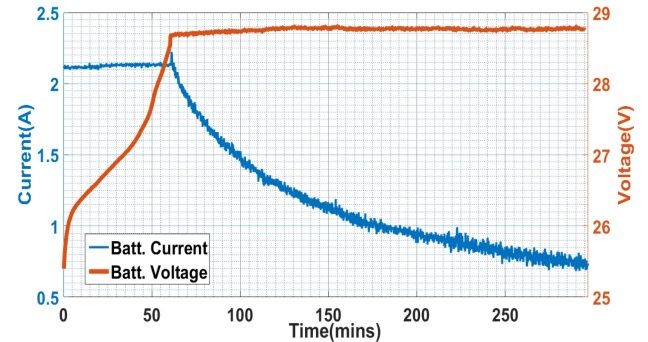


Fig. 25. Obtained V-I curve from CC-CV charging of 24 V, 30 Ah lead acid battery with R-OPC.

While charging the battery, the power factor varies from 0.99 at the beginning to 0.96 at the end of charging. Similarly, the THD of input current is found to be 13.8% at the beginning and 23.2% at the end.

### B. Impact of Reconfiguration

The objective of reconfiguration is to increase the power density by reducing the number of power electronic components without significantly affecting efficiency. The proposed reconfigurable topology achieves this by reutilizing the 3-phase VSI in the charging mode.

*1) Component Utilization Factor:* The component utilization factor (CUF) for multimode operation, as in this case, may be expressed separately for the different modes since the precise duration of each mode is not specified. The CUF, as defined in [34], is the ratio of minimum number of components required for operation with respect to the actual number of components.

$$\text{CUF} = \frac{\text{Minimum number of required components}}{\text{Actual number of components}} \quad (15)$$

The CUF of the proposed converter as well as the on-board battery charger topologies available in literature are calculated on the basis of (15). Henceforth, they are compared in Table IV.

TABLE IV  
COMPARISON OF COMPONENT UTILIZATION FACTOR OF PROPOSED TOPOLOGY WITH EXISTING LITERATURE

Sl. No.	Literature	Total number of switches (n)	Switches used during charging mode (c)	Switches used during propulsion mode (p)	Charging CUF (c/n)	Propulsion CUF (p/n)
1	[13]	10	10	6	1	0.6
2	[14]	18	18	6	1	0.333
3	[15]	22	16	6	0.7272	0.2727
4	[24]	10	10	6	1	0.6
5	[25]	21	21	6	1	0.2857
6	Proposed	8	8	6	1	0.75

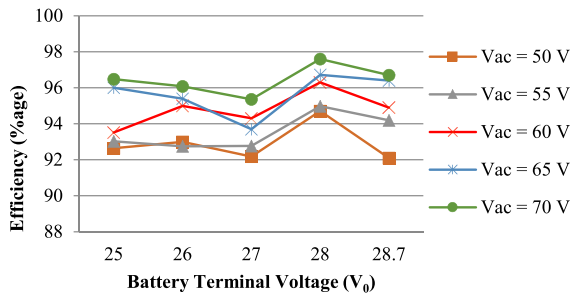


Fig. 26. Efficiency curves for different input voltages.

It is observed from Table IV that the CUF in charging mode is unity in all except for [15]. However, the CUF in propulsion mode is considerably improved in the proposed topology. Further, the duration of charging is generally less than the duration of propulsion mode. Therefore, it can be inferred that the overall CUF has been improved.

2) *Power Density Analysis:* In case of an on-board charger, it is necessary to carry out the power density analysis as the volume of the power processor plays an important role. Power density can be improved by optimizing certain circuit design parameters [35]. The approach of reconfiguration proposed in this work achieves the same goal on a significant scale. The topology integrates the battery charger and the propulsion unit into a single converter eliminating the requirement of a separate 3-phase VSI. A scaled-down laboratory prototype is developed as shown in Fig. 15. The volume of the experimental prototype for the proposed topology is measured to be  $9.177 \text{ dm}^3$ . The power density for proposed topology rated at 470 W is measured as  $51.2 \text{ KW/m}^3$ .

3) *Efficiency Analysis:* The measured efficiency of the proposed prototype at different input AC voltages over the complete range of battery terminal voltage during charging of a 24 V battery pack is presented in Fig. 26. It can be inferred from Fig. 26 that the efficiency improves with increasing input AC voltage. However, the input voltage magnitude is limited by the rating of the experimental setup. The peak efficiency achieved is 97.6% during charging at an input AC voltage of 70 V (rms).

## VI. CONCLUSION

A Reconfigurable On-board Power Converter (R-OPC) for low battery voltage EVs is presented in this paper. A 3-phase, 6-switch VSI is reconfigured to serve both charging and propulsion of the EV, thus improving the overall power density of the on-board charger. The detailed operation of the proposed R-OPC in both charging and propulsion mode presented in the paper. The motor phase windings are reutilized as circuit inductances during charging mode which further improves the power density of the topology. Mode transition is achieved with the help of sequential switching of contactors. The contactors are operated in zero current condition eliminating switching loss during mode transition. The proposed approach achieves improvement in power density and reduction in switch count as compared to recent literatures presenting contemporary power converters for EVs. A unified control loop scheme capable of near-unity power factor operation at the input stage and performing optimal charging (CC-CV) of the battery in one single control loop is also implemented. A 470 W prototype is developed to validate the performance of the proposed R-OPC. The proposed R-OPC is also validated with CC-CV charging of a 24 V, 30 Ah lead acid battery.

## REFERENCES

- [1] S. Li, L. Tong, J. Xing, and Y. Zhou, "The market for electric vehicles: Indirect network effects and policy design," *J. Assoc. Environmental Resour. Economists*, vol. 4, no. 1, pp. 89–133, 2017.
- [2] W. Sierczula, S. Bakker, K. Maat, and B. van Wee, "The influence of financial incentives and other socio-economic factors on electric vehicle adoption," *Energy Policy*, vol. 68, pp. 183–194, 2014.
- [3] A. Khaligh and S. Dusmez, "Comprehensive topological analysis of conductive and inductive charging solutions for plug-in electric vehicles," *IEEE Trans. Veh. Technol.*, vol. 61, no. 8, pp. 3475–3489, Oct. 2012.
- [4] M. Yilmaz and P. T. Krein, "Review of battery charger topologies, charging power levels, and infrastructure for plug-in electric and hybrid vehicles," *IEEE Trans. Veh. Technol.*, vol. 28, no. 5, pp. 2151–2169, May 2013.
- [5] V. Monteiro, H. Gonçalves, J. C. Ferreira, and J. L. Afonso, "Batteries charging systems for electric and plug-in hybrid electric vehicles," in *New Advances in Vehicular Technology and Automotive Engineering*, 1st ed., J. P. Carmo and J. E. Ribeiro, Eds., Rijeka, Croatia: InTech, 2012, pp. 149–168.
- [6] J. Wirtz, "On-board vs. Off board charging," *Elect. Transp. Infrastruct.*, Eaton Corp., Milwaukee, WI, USA, Tech. Rep., 2011.

- [7] Plugged in: How Americans charge their electric vehicles, Idaho National Laboratory, Idaho Falls, ID, USA, Tech. Rep., Dec. 2015.
- [8] M. A. Hans Bngtsson, "Cost analysis of electric land transport," Swedish Electric & Hybrid Vehicle Centre, Chalmers Univ. Technol. Horsalsvagen, Sweden, Tech. Rep., Jun. 2015.
- [9] M. Yilmaz and P. T. Krein, "Review of integrated charging methods for plug-in electric and hybrid vehicles," in *Proc. IEEE Int. Conf. Veh. Electron. Safety*, Jul. 2012, pp. 346–351.
- [10] N. Sakr, D. Sadarnac, and A. Gascher, "A review of on-board integrated chargers for electric vehicles," in *Proc. 16th Eur. Conf. Power Electron. Appl.*, Aug. 2014, pp. 1–10.
- [11] S. Haghbin, S. Lundmark, M. Alakula, and O. Carlson, "Grid-connected integrated battery chargers in vehicle applications: Review and new solution," *IEEE Trans. Ind. Electron.*, vol. 60, no. 2, pp. 459–473, Feb. 2013.
- [12] A. Cocconi, "Combined motor drive and battery recharge system," U.S. Patent 5 341 075, Aug. 1994.
- [13] G. Pellegrino, E. Armando, and P. Guglielmi, "An integral battery charger with power factor correction for electric scooter," *IEEE Trans. Power Electron.*, vol. 25, no. 3, pp. 751–759, Mar. 2010.
- [14] C. Shi, Y. Tang, and A. Khaligh, "A three-phase integrated onboard charger for plug-in electric vehicles," *IEEE Trans. Power Electron.*, vol. 33, no. 6, pp. 4716–4725, Jun. 2018.
- [15] H. Wang, S. Dusmez and A. Khaligh, "Design and analysis of a full-bridge LLC-based PEV charger optimized for wide battery voltage range," *IEEE Trans. Veh. Technol.*, vol. 63, no. 4, pp. 1603–1613, May 2014.
- [16] I. Subotic, N. Bodo, and E. Levi, "An EV drive-train with integrated fast charging capability," *IEEE Trans. Power Electron.*, vol. 31, no. 2, pp. 1461–1471, Feb. 2016.
- [17] I. Subotic, N. Bodo, E. Levi, and M. Jones, "Onboard integrated battery charger for EVs using an asymmetrical nine-phase machine," *IEEE Trans. Ind. Electron.*, vol. 62, no. 5, pp. 3285–3295, May 2015.
- [18] M. S. Diab, A. A. Elserougi, A. S. Abdel-Khalik, A. M. Massoud, and S. Ahmed, "A nine-switch-converter-based integrated motor drive and battery charger system for EVs using symmetrical six-phase machines," *IEEE Trans. Ind. Electron.*, vol. 63, no. 9, pp. 5326–5335, Sep. 2016.
- [19] I. Subotic, N. Bodo, and E. Levi, "Single-phase on-board integrated battery chargers for EVs based on multiphase machines," *IEEE Trans. Power Electron.*, vol. 31, no. 9, pp. 6511–6523, Sep. 2016.
- [20] I. Subotic, N. Bodo, E. Levi, M. Jones, and V. Levi, "Isolated chargers for evs incorporating six-phase machines," *IEEE Trans. Ind. Electron.*, vol. 63, no. 1, pp. 653–664, Jan. 2016.
- [21] I. Subotic, N. Bodo, E. Levi, B. Dumnic, D. Milicevic, and V. Katic, "Overview of fast on-board integrated battery chargers for electric vehicles based on multiphase machines and power electronics," *IET Electric Power Appl.*, vol. 10, no. 3, pp. 217–229, Mar. 2016.
- [22] S. Dusmez and A. Khaligh, "A compact and integrated multifunctional power electronic interface for plug-in electric vehicles," *IEEE Trans. Power Electron.*, vol. 28, no. 12, pp. 5690–5701, Dec. 2013.
- [23] H. Choi, "Half-bridge LLC resonant converter design using FSFR-series Fairchild power switch (FPS)," ON Semiconductor, Aurora, CO, USA, Tech. Rep. AN-4151, Oct. 2007.
- [24] C. Shi, Y. Tang, and A. Khaligh, "A single-phase integrated onboard battery charger using propulsion system for plug-in electric vehicles," *IEEE Trans. Veh. Technol.*, vol. 66, no. 12, pp. 10899–10910, Dec. 2017.
- [25] C. Shi and A. Khaligh, "A two-stage three-phase integrated charger for electric vehicles with dual cascaded control strategy," *IEEE J. Emerg. Sel. Topics Power Electron.*, vol. 6, no. 2, pp. 898–909, Jun. 2018.
- [26] R. W. Erickson and D. Maksimovic, *Fundamentals of Power Electronics*, 2nd ed., New York, NY, USA: Springer Science + Business Media, 2001.
- [27] P. Wang, C. Liu, and L. Guo, "Modeling and simulation of full-bridge series resonant converter based on generalized state space averaging," in *Instruments, Measurement, Electronics and Information Engineering* (series Applied Mechanics and Materials), vol. 347. Zurich, Switzerland: Trans Tech Publications, pp. 1828–1832, Oct. 2013.
- [28] E. X.-Q. Yang, "Extended describing function method for small-signal modeling of resonant and multi-resonant converters," Ph.D. dissertation, Virginia Polytechnic Institute and State University, Blacksburg, 2005.
- [29] H. Huang, "Feedback loop design of an LLC resonant power converter," Texas Instruments, Dallas, TX, USA, Tech. Rep. SLUA582A, Oct. 2010.
- [30] J. Lu, A. Mallik, S. Zou, and A. Khaligh, "Variable DC-Link control loop design for an integrated two-stage AC/DC converter," *IEEE Trans. Transp. Electricif.*, vol. 4, no. 1, pp. 99–107, Mar. 2018.
- [31] L.-R. Chen, "Design of duty-varied voltage pulse charger for improving Li-ion battery-charging response," *IEEE Trans. Ind. Electron.*, vol. 56, no. 2, pp. 480–487, Feb. 2009.
- [32] L.-R. Chen, N.-Y. Chu, C.-S. Wang, and R.-H. Liang, "Design of a reflex based bidirectional converter with the energy recovery function," *IEEE Trans. Ind. Electron.*, vol. 55, no. 8, pp. 3022–3029, Aug. 2008.
- [33] A. Al-Haj Hussein and I. Batarseh, "A review of charging algorithms for nickel and lithium battery chargers," *IEEE Trans. Veh. Technol.*, vol. 60, no. 3, pp. 830–838, Mar. 2011.
- [34] M. M. Jovanovic, "Dual AC-input power system architectures," in *Proc. APEC. 17 Annu. IEEE Appl. Power Electron. Conf. Expo. (Cat. No.02CH37335)*, Dallas, TX, USA, 2002, vol. 1, pp. 584–589.
- [35] I. Laird, X. Yuan, J. Scoltock, and A. J. Forsyth, "A design optimization tool for maximizing the power density of 3-Phase DC-AC converters using silicon carbide (SiC) devices," *IEEE Trans. Power Electron.*, vol. 33, no. 4, pp. 2913–2932, Apr. 2018.



**Soumya Ranjan Meher** (Student Member, IEEE) received the B.Tech. degree in electrical and electronics engineering from the Biju Patnaik University of Technology, Odisha, India, in 2012, the M.Tech. degree in renewable energy and energy management from the National Institute of Technology, Arunachal Pradesh, India, in 2017. He is currently working toward the Ph.D. degree with the Department of Electrical Engineering, Indian Institute of Technology (Banaras Hindu University), Varanasi, India. His research interests include power processor design for electric vehicle, modeling and control of soft switching converters, optimal battery charging.



**Somenath Banerjee** (Student Member, IEEE) received the B.Tech. degree in electrical engineering from the Maulana Abul Kalam Azad University of Technology, Kolkata, India, in 2017 and the M.Tech. degree in power electronics from the Indian Institute of Technology, Banaras Hindu University, Varanasi, India, in 2019. His research interests include converter modeling and control, soft switching converters, and battery charging for electric vehicles.



at Dallas, Richardson, TX, USA, in WBG semiconductor reliability. His research interests include WBG device applications, WBG reliability, converter design, and embedded control.



**Rajeev Kumar Singh** (Senior Member, IEEE) received the B.Tech. degree in electrical engineering from the College of Technology, Pantnagar, India, in 2001, the M.Tech. degree in electrical machines and drives from the Indian Institute of Technology (Banaras Hindu University), Varanasi, India, in 2003, and the Ph.D. degree in electrical engineering from the Indian Institute of Technology Kanpur, Kanpur, India, in 2013. He is currently an Associate Professor with the Department of Electrical Engineering, Indian Institute of Technology (Banaras Hindu University). His research interests include renewable power conversion for hybrid microgrid, power conversion for electric vehicles/hybrid electric vehicles, optimal charging/discharging of energy storage system, and converter modeling and control.